SIMULATION OF HYDRAZINE MICROTHRUSTER FEED TUBE CLOGGING

by

Felicissimo Jose da Silva Filho

B.S. Military Institute of Engineering
Rio De Janeiro, Brazil (1970)

Submitted in Partial Fulfillment
of the Requirements for the
Degree of

MASTER OF SCIENCE
IN AERONAUTICS AND ASTRONAUTICS

at the

MASSACHUSETTS INSTITUTE OF TECHNOLOGY

December 1982

Signature redacted

Signature of Author.....
Department of Aeronautics and Astronautics,
December 17, 1982

Signature redacted

Certified by.....
Manuel Martinez Sanchez, Thesis Supervisor

Signature redacted

Accepted by.....
Harold Y. Wachman, Chairman, Departmental Graduate Committee

SIMULATION OF HYDRAZINE MICROTHRUSTER

FEED TUBE CLOGGING

by

Felicissimo Jose da Silva Filho

Submitted to the Department of Aeronautics and Astronautics on December 22, 1982 in Partial Fulfillment of the Requirements for the Degree of Master of Science

ABSTRACT

An experimental study was carried out on the clogging of Hydrazine Microthruster Feed Tubes by Non-Volatile Residues. The study consisted of a simulation test using a solution of $CaSO_4$ in Deionized water supplied by a stainless steel tank under pressure. A 7.30 hours test was run with flow starting at 12 cc/min at that concentration.

The geometry of the chamber and injector heads closely parallels that of the HIPEHT engines used on INTELSAT V, except that the injection capillary has about half the wall thickness of the VD Rh tubes on HIPEHT.

NiCr heating wire was used on the outside of the chamber to get sufficient power to induce boiling in the injector.

The most important results of data suggest similar plugging behavior in water/stainless steel as in hydrazine/VDR or Pt. This is supportive of a physical (boiling) mechanism inside the injector capillary, 5 to 10 diameters ahead of the conical end of the chamber.

Thesis Supervisor: Manuel Martinez Sanchez
Title: Associate Professor of Aeronautics and Astronautics

ACKNOWLEDGEMENTS

The author would like to express his gratitude for the technical support and advice of the following people throughout this research effort: Professor Clifton G. Fonstad, Jr., Mr. E. Don Weiner, Mr. Viktor Dubrowski, Mr. John N. Stanley and Mr. George H. Leach. Also, my advisor Professor Manuel Martinez Sanchez is thanked for his unfailling support and confidence in my ability to successfully complete this effort. A very special thanks is reserved for Dr. Paul E. Brown of C.A.E.S. who supported and adviced me since I arrived at MIT.

TABLE OF CONTENTS

LIST OF TABLES

LIST OF FIGURES

LIST OF SYMBOLS

A_w Cross-sectional area of the wall.

C_l Fluid specific heat.

C_{sf} Dimensionless constant, depends on liquid-surface pair.

C_v Vapor specific heat.

D_0 Capillary outside diameter.

d Capillary inside diameter.

d_h Hydrazine density.

d_l Liquid density.

d_r Residue density.

d_v Vapor density.

d_w Water density.

F Factor near unity, accounting for properity variability.

h_{fg} Latent heat.

I_{sp} Specific impulse (seconds).

K_l Liquid thermal conductivity.

K_v Vapor thermal conductivity.

K_w Wall thermal conductivity.

m_p Plug mass.

Max Maximum.

NVR Non-volatile residue.

P Pressure.

P_c Chamber pressure.

P_r Prandtl number.

P_T Tank pressure.

P_w Wetted perimeter of wall.

ΔP The pressure difference between supply tank and chamber.

Q Measured flow rate.

$\dot{q}$ Heat flux from wall to fluid.

Q_c Total heat flow on wall.

r_{inner} Capillary radius.

REC Recommended.

R_e Reynolds number.

R_g Gas constant for vapor.

T Temperature (°K)

t Time (min).

t_w Wall thickness.

u Liquid velocity.

η_d Deposition efficiency.

δ Thickness of thermal layer.

σ Surface tension.

Chapter 1

INTRODUCTION

1.1 Introduction

Deposition on heated surfaces is a commonly encountered process. The formation of boiler scale in steam boilers is an example of great technical and economic interest. The main mechanism of scale formation is the concentration of salts at points where steam bubbles form during nucleate boiling. This precipitation forms a scale or deposit whose adherence may be enhanced by the high temperature of the heater element. If all the liquid is vaporized, then all the salts and other non-volaties are left behind as a deposit.

The augmented electrothermal thruster developed by TRW, called HIPEHT for INTELSAT V (1) undergoes a decrease in flow rate before mission life is completed. Solid material is deposited in the feed tube during the operation and eventually the flow of the liquid hydrazine is restricted excessively. The details of the mechanism are not understood, so correction and, or improvement is hampered. As the size of these thrusters has been reduced and the hydrazine throughput increased, several of them have experienced progressive, and sometimes sudden, flow degradation with time (1). Almost universally, the problem appears near the hot end of the tube, some 5-10 diameters (1-2 mm) ahead of the attachment to the hot decomposition chamber.

There are many three-axis stabilized spacecraft that require the

use of low level hydrazine thrusters (operating at 0.2 lbf or less) for various phases of on-orbit attitude and velocity control (2). Some of these flight applications require very high mass throughputs for individual low level thrusters (3). However, test results from long duration, low level thruster firings indicate a sensivity of thruster performance to deposition of trace impurities from the flowing hydrazine. Performance degradation has been observed in small thrusters, where a build up of these impurity deposits tends to occur in the internal passageway of the injector feed tube. This flow blockage causes reductions in thrust and delivered impulse as well as other performance losses (1).

At the 0.2 lbf thrust level (or lower), the internal diameter of injector feed tube is typically 0.005 to 0.012 inches. These small passages have demonstrated a high susceptibility to flow blockage from deposits of extraneous matter in the hydrazine. Test results accumulated thus far indicate that the tendency for this flow blockage phenomenon to occur is related to thruster thermal design, materials of construction, firing duration, flow rates, pressure levels, hydrazine quality, and other design and operating details.

Additional complications have been observed for small hydrazine thrusters that use electrothermal energy for performance augmentation (4). This is because the specific power requirement for augmentation of Isp into the 300 second range (on the order of 5 watts per millipound of thrust) usually requires that the upper bound for thrust be maintained at 0.1 lbf or less. These lower thrust levels,

combined with generally higher operating temperature, tend to increase the occurrence of material build up in electrothermally augmented thruster feed tubes.

There are a number of flight applications of low thrust hydrazine engines. These applications include attitude control, and station keeping maneuvers for interplanetary probes such as Voyager 1977. Low thrust propulsion systems are flown on NASA and commercial space payloads (1). A summary of current flight applications is presented in Table 1.1 (taken from reference (1)).

The hydrazine used in the HIPEHT is highly purified. Even the exceedingly low non-volatile residue (NVR) quantity of 20 parts per million is sufficient to block the feed tube many times over. It seems likely that other thrusters (i.e. catalytic hydrazine) have also encountered deposition, but very few thrusters flow enough propellant through small enough feed passages to restrict flow rate significantly. The normal chemical analysis of impurities dissolved in hydrazine covers iron, chloride, carbon dioxide and particulates (1). Additionally, the solid remaining after evaporating a large amount of liquid is weighted and report as NVR. Carbon dioxide is really bound to hydrazine as carbazic acid or carbazate salt. The salts and their decomposition products and the NVR are candidates for deposition. Most of NVR in hydrazine is in the propellant before purification. The zone purification process currently being used to refine hydrazine apparently does not introduce any new chemical species but merely reduces the total NVR content. This process is capable of producing

hydrazine with a total NVR content of the order of 1 ppm. Table 1.2 compares the NVR for four grades of hydrazine. The nature of the deposits is variable but oxides and nitrides of iron and calcium seem to prevail. The best grade of hydrazine is used with only a few ppm of impurities and further purification is difficult. Besides the region of blocking is so localized, that even at 1 ppm there is plenty of material in the large hydrazine throughput to effect clogging. For instance, taking a plug of 10 diameters with $dr \simeq 3\ g/cm^3$ and $r = 10^{-4}m$ we have $mp = 1.9 \times 10^{-7}Kg$. Since a 10 year NSSK (North/South Station Keeping) mission with 1000 Kg payload per thruster means ~ 160 Kg of hydrazine, the plug requires only 1.2×10^{-9} concentration of non-volatile residues. Even with 0.1 ppm NVR there is over 100 times more than needed for plugging. Some deposition must occur upon shutdown of a thruster wherein the heat soak and ambient vacuum vaporize all the liquid downstream of the valve. HIPEHTs usually fire for long durations so there are few shutdowns and shutdown heat soak is considered to be a minor contributor. Material has been reported to deposit during continuous operation. It had been postulated at one time that the liquid flowing in steady-state in the feed tube vaporized, leaving the non-volatiles (5).

Calculations have shown much less heat transfers from the thruster through the feed tube to the liquid than the heat needed to vaporize all the liquid. Even though no bulk boiling is predicted, subcooled nucleate and film boiling can occur in the feed tube close to the chamber. So, the operating mode is found to influence the detailed course of the blockage if frequent starts and stops occur, favoring

eventual clogging by particles dislodged from the valve or upstream lines during transients. Similar effects occur if the feed tank is repressurized after partial blowdown.

Nucleate boiling occurs on walls slightly above the saturation temperature of the liquid. The rapid growth and collapse of bubbles induces great liquid activity at the hot wall and transfers high heat fluxes. At some higher heat flux value the bubbles coalesce and form an insulating layer of vapor and the wall temperature rises rapidly at the onset of film boiling. This flux value is called the upper limit of nucleate boiling. Even at these high fluxes, there is insufficient heat transferred to the HIPEHT feed tube to raise all the liquid to its boiling point. The boiling process is probably distorted in the HIPEHT feed tube by the small passage; the 0.2 mm tube diameter is smaller than typical nucleate boiling bubbles. However, a detailed analysis of the flow and heat transfer characteristics in the feed tube leads to the prediction of highly localized subcooled boiling with vapor bubbles only a few microns in diameter (6).

In order to produce quantitative data on flow degradation under conditions closely resembling those in the HIPEHT engine, excepting the chemistry, an apparatus was designed and assembled using deionized water and calcium sulfate as NVR agent for simulation of the hydrazine flow system in the HIPEHT.

Chapter 2 contains a brief description of the experimental equipment acquired and facility used. Chapter 3 describes the preliminary procedures as well as a detailed discussion of the experimental results.

A summary of this research effort with conclusions and recommendations for further research are presented in Chapter 4.

1.2 Historical Data

Reduction of propellant flow in small injector tubes (thrust level of less than 0.5 lbf) has occurred during thruster development, qualification testing and on-orbit operation. This has been attributed primarily to particulate contamination due to inadequate hardware cleanliness control and deposition of non-volatile (NVR) contained in trace quantities in the propellant.

Table 1.3 summarizes some of the more recent occurrences of flow degradation due to NVR (1)(7)(8).

Perhaps the first time that flow blockage from NVR deposition was recognized as such, occurred in a thruster being evaluated for the Thermoelectric Outer Planets Spacecraft (TOPS) research and development program at JPL (9). Iron, calcium and potassium were found in the deposit in the L-605 tube but calcium and potassium were not recognized at that time as having come from the hydrazine. One very interesting aspect of this flow blockage is that it occurred three different times on the same thruster. The tube was cleared with a wire the first two times so that the flow rate of the tube returned to normal. The tube was cut apart and the deposit was analyzed after the third flow blockage.

Rocket Research Corporation (RRC) measured thrust degradation rates as high as 0.6 percent loss per hour at 350 psia inlet pressure during

LCSSE/VGR steady-state life margin tests on a 0.2 lbf catalytic thruster (10). The degradation was attributed to trace quantities of silicon and iron in the propellant which deposited in the feed tube during life tests. As a result, tighter control of these constituents in the propellant has been recommended by RRC (10).

During development and qualification of the High Performance Electrothermal Hydrazine Thruster (HIPEHT) for the Intelsat V satellite, TRW measured some flow reduction due to NVR deposition for steady-state hydrazine throughputs between 50 and 185 pounds.

Two 0.2 lbf catalytic thrusters from the Voyager 1977 program were provided to TRW by JPL for sectioning and comparison with TRW's HIPHET data (11). The two thrusters, S/N 025 and 043, were reported to have experienced 45 percent thrust degradation after 53 pounds (S/N 025 pulse mode duty cycle) and 160 pounds (S/N 043 steady-state mode duty cycle) of hydrazine throughput. The deposition area in the steady-state unit was very similar in appearance, general location and NVR content to the TRW HIPEHT units, indicating NVR deposition is a common problem with both catalytic and electrothermal thrusters. Major NVR constituents measured by electron beam microprobe analysis were iron, silicon, calcium and potassium. The other Voyager thruster which was fired predominantly in the pulse mode (33% duty cycle) exhibited nitriding of the Inconel tube and cracking of the nitrided layer in addition to NVR deposition. This was to be expected based on the duty cycle and feed tube material. Both thrusters were fired with propellant that had been stored in a titanium tank containing an AFE-332 diaphragm for one year. Pre-test and post-test analysis of the propellant showed

no out-of-specification NVR content.

The ATS-G spacecraft has experienced plugged, stuck open and flow-degraded thrusters on-orbit. Potential mechanisms identified for the thruster anomalies are particulate contamination, propellant contamination from the tank diaphragms and NVR deposition (12).

Test and flight experience indicate the blockage is probably more influenced by thermal, chemical and material interactions within the feed tube and injector rather than simply contamination from sources such as tank diaphragms and system particulate. Mission life tests were conducted by TRW on the MRE .2 (0.2 lbf) catalytic thruster with propellant supplied directly from a flight tank containing an AFE-332 diaphragm after 6 months storage at 160°F. Post-test performance compared favorably with identical tests on other thrusters fired from facility tankage indicating no measureable effects of AFE-332 diaphragm on thruster operation. (The seven paragraphs above were taken literally from reference 1).

At MIT, an experimental characterization of the non-volatile residue (NVR) clogging phenomenon was carried out, under the working hypothesis that physical, as opposed to chemical phenomena are responsible for it (13). This experiment was meant to produce quantitative data on flow degradation under conditions closely resembling those in the HIPEHT engine (excepting the chemistry). Hydrazine flow was simulated using water soluble salts, based on the fact that water has almost the same physical properties as hydrazine, as observed in Table 1.4. The one significant difference is its thermal conductivity.

Some results of the MIT tests can be seen in Figure 2.1 and a flow degradation of the order of 5 percent is apparent after 6 hours of flow at 0.17 g/sec.

To understand, the flow degradation data generated by ground test and flight operation, the specific thruster temperature profiles, materials, flow regimes, duty cycle and propellant condition must be examined in detail to identify the controlling parameters.

Chapter 2

EXPERIMENTAL EQUIPMENT AND PROCEDURE

2.1 Introduction

At the present day one has available many alternative ways of performing a measurement. These often differ in the scientific principle on which the apparatus is based, the mechanism through which this principle is applied, and the way in which the result is displayed. The experimental equipment listed below was evaluated considering the factors: resolution, accuracy, convenience and cost which were sufficient factors to the apparatus to perform well.

2.2 Vacuum Pump

This study was done in the MIT NRC MODEL 3116 VACUUM COATER available at the Gas Turbine Laboratory. The Model 3116 system consists of a bell jar vacuum chamber; a counterbalanced bell jar hoist; a baseplate with electrical feed throughs; a complete vacuum pumping system, with controls and gauging. The baseplate contains the main pumping port and twelve identically sized feed holes. Filament electrodes are installed in four of these holes; the remaining eight are filled with removable O-ring sealed plugs for additions. Using only the mechanical vacuum pump one achieved a vacuum of 250 μm. Due to vibration of the equipment structure caused by the mechanical pump, difficulties were encountered in bringing the electrical power to the very fine heater wire at the junction of both.

2.3 Transformer and Heater

The experiment used a STACO Portable Variable Autotransformer Model 3PN1210, 0-120 VAC at 12 amps, that provided continuously adjustable output voltage from the AC power source without wave form distortions to the heater wire.

The electric heater was AEROCOAX Model 1HM-040F-16.3 with the specifications presented in Table 1.5. This cable is made by a multiple pass drawing operation. When shipped, the ends are sealed to prevent moisture absorption by the MgO insulation. Once the seal is broken, the MgO will absorb moisture from the atmosphere and rapid loss of insulation resistance and dielectric strength can occur. Destructive arcing between the wire and sheath can occur if the wet cable is energized. Unsealed cable can be dried by a 24 hour oven bakeout at 250°F or higher or by self-heating at low voltage.

In general, there is very little temperature difference between the sheath and wire. With the cable sheath operating at temperatures less than 1000°F it is recommended not to exceed 150 watts/square inch. As temperature increases above 1000°F, the maximum watt density should be decreased. Maximum recommended operating temperature is 1500°F. Above this temperature, the stainless steel sheath will begin to rapidly oxidize in air. However, since the experiment was performed in vacuum, this problem was circumvented. Also, due to the effective water cooling, power densities well above the stated limit were attained.

2.4 Thermocouple and Multitester

The temperature sensing element should be in good contact with the wall and should have a two-dimensional rather than a three-dimensional extension because the thermal junction in a two dimensional plane can offer precise depth information on the point of temperature measurement.

The temperature-sensing element must not produce a disturbance in the flow at the measuring point. Such a disturbance would cause shock waves in supersonic flow and change entirely the thermal conditions at the wall surface. In compressible flow the thermal junction must be mounted flush with the surface.

The two-dimensional thermal junction NANMAC Model A13-2 bare thermocouple with specifications in Table 1.6 was used in this experiment.

The multitester utilized was the KEITHLEY Model 169 Digital Multimeter. It is a, battery operated digital multimeter that provides full measurement capability for many general purpose applications. It provides readings from V/digit to 1000 V on five DC and five AC current ranges, and 100 mohms/digit to 20 megohms on six resistance ranges. Through the Figure 2.2 one can get the correspondent temperature in °F.

2.5 Injector, Chamber and Nozzle

The geometry of the injector capillary and chamber heads closely parallels that of the HIPEHT engines, except that injection capillary whose specifications are in Table 1.7 has about half the wall thickness

of the VD Rh tubes. The impact of this and other small differences were discussed in reference 6 and is expected to be mainly a shortening of distance from the NVR deposition point to the injector end. The capillary wall thickness availabe are significantly less than those typical of HIPEHT designs (14/1000 inches stainless steel or more). In addition, the thermal conductivity of stainless steel is about 1.6 times below that of Rh. Since the axial distance from the injector hot end varies for a given wall temperature, the substitution will lead to a shortening by approximately 1/1.5 of the distance to the point of deposition. Some additional shortening is expected from the higher thermal conductivity of water as compared to hydrazine (14,15). This estimates are quantified more precisely in Section 3.3.

In Figures 2.3 and 2.4 the chamber (similar to that one of the HIPEHT) and the 0.63 mm exhaust nozzle are seen in separated design, but these components were assembled with the nozzle orifice side brazed to that flat end of the chamber. Seven turns of NiCr heating wire were also brazed to the outside of the chamber, and so was a 5 mil Iron-Constantan thermocouple attached to the conical side of the chamber.

2.6 Tank, Filters and Flowmeter

The schematic of the instrumentation and equipment used is shown in Figure 2.5, which also illustrates the placement of the tank, filters and flowmeter in the system. The 10 liters water tank used was a stainless steel cylinder with flat ends and two feed throughs for pressurization by nitrogen from a standard gas bottle.

The two filters are NUPRO B-4TF-7 and B-4TF-60, and provided the remotion of contamination as small as seven and sixty microns before the the injector capillary and before the flowmeter respectively.

In this type of filter the fluid passes from the outside area of the filter element to the inside. This provides a large effective filtering area and eliminates the possibility of the element being unseated due to pressure build up or pulsations. The element traps contamination, allowing the cleaned fluid to pass through the system. The flowmeter utilized to measure the water flow rate was a 0-16 cc/min Fischer Porter Flowmeter.

The selection of solutes for this NVR simulation test obeyed the following requirements for a suitable test contaminant for NVR deposition (14):

1. It should precipitate upon boiling.
2. Its stability must be small in ordinary water, to prevent reentrainment of deposits.
3. The deposits should form a tenacious crust on the boiling surface.
4. It should be possible to prepare solutions of enough concentration to produce substantial deposition in less than 8 hours of running.

Calcium sulfate, present in some natural waters is known (16) to accelerate boiler incrustation. Its solubility is greater than that of the carbonate (except at CO_2 pressures over two atmospheres), and decreases with temperature as well, at least above 35°C.

An additional advantage of this salt is that its solubility is

independent of pressure and gas composition, thus facilitating operations and interpretation. A possible problem is the observation that the non-adhering precipitate is a relatively coarse dust, with microcrystals of about 0.08 mm diameter. It is hoped, however, that the very short time available for growth under the flow conditions will prevent this size grain from forming in the injector capillary. If the deposition efficiency is assumed to be η_d, the NVR concentration, in parts per million, required to grow a crust of thickness δ_c in a time t can be estimated by the formula (15)

$$(PPM) = \frac{10^6(\delta_c/t)h_{fg}d_r}{\eta_d\, q_b}$$

where h_{fg} is the heat of vaporization of water, d_r the density of the deposited residue and q_b the average wall heat flux in the boiling region. The feed tubes used have an i.d. of 0.178 mm (7/1000"), so substantial plugging will occur when $\delta \simeq 0.040$ mm. Using h_{fg} = 540 cal/g, $d_r \simeq 2$ g/cm^3, $q_b \simeq 5 \times 10^6$ w/m^2, and assuming a run time of 4 hours, we obtain

$$(PPM) = \frac{2.52}{\eta_d}$$

From HIPEHT data η_d seems to be about 10 percent; this experiment $CaSO_4$ boiling test would support values between 1 and 10 percent on stainless steel. Thus, between 25 and 250 ppm are required in the solution, well below the $CaSO_4$ room temperature solubility (2000 ppm).

Chapter 3

EXPERIMENTAL RESULTS AND DISCUSSION

3.1 Introduction

The effects of the $CaSO_4$ solution in deionized water simulating the hydrazine microthrusters feed injector were studied.

Temperature, pressure and flow rate at the chamber were noted every 10 minutes to present the results of the experiment.

The chamber temperature was measured with a bare thermocouple located at the conical end (upstream) of the chamber, near the attachment of the injector capillary to the chamber.

For the condition of this test one can see that the shape of the degradation flow curve is a direct function of the flow characteristics of the deposition as in Figure 2.6, a general case, where a venturi-type deposit was assumed with a flow coeficient (c_v) of 0.9.

It is postulated in these results that at the point of incipient boiling a small portion of NVR from calcium sulfate solution is deposited onto the injector capillary wall as shown in Figure 2.7. This was confirmed by past-test analysis of the plugged capillary. (See Section 1.2).

3.2 The Experiment

Table 1.8 is the raw data sheet for a run that used a 150 ppm solution of calcium sulfate, starting the test with a 12 cc/mm flow rate.

The temperature and pressure characteristics of the injector capillary in this study ran close to that general temperature and pressure characteristics case of a propellant feed tube during a steady state firing as illustrated in Figure 2.8.

The temperature data obtained with a bare type J thermocouple wire are of limited absolute accuracy due to uncertainties regarding radiation inside the vacuum bell jar whose mechanical vacuum pump provided a 250 μm of Hg vacuum. The seven turns of heater wire were seen directly by the junction. However, these data played an important diagnostic role during the test. The water calcium sulfate solution temperature was initially restricted to 100°C at the chamber (with the pressure varying between four and six atmospheres) to avoid the boiling point around 150°C at five atmospheres. Under these conditions the first point noted in the data sheet of Table 1.8 was obtained. This pressure range at the chamber was maintained through slight adjustments of the downstream valve shown in Figure 2.5.

After this first point noted the temperature of the chamber jumped from 207°C to 500°C and the chamber pressure became higher, requiring more significant adjustment of the downstream valve to maintain the chamber pressure as close as possible to five atmospheres. It was found

that the two operating regimes were separated by a clear threshold, that existed during the 120 minutes from starting point. The average chamber pressure was then six atmospheres and the heater power inputs varied between 20.0 and 22.8 volts. The electric power was regulated with a variable autotransformer and measured by the applied rms voltage.

During these 120 minutes, the temperature readings fluctuated between about 22 mV and 29 mV (424°C to 550°C) in times of the order of seconds and in a random pattern. Above the threshold, a stable temperature of 29 mV (550°C) was obtained increasing in a regular and predictable way with further voltage increases. This was interpreted as evidence that complete dryout of the chamber water was not achieved below threshold, so that splashing occurred and was evidenced in the temperature fluctuation. The data for the first 120 minutes show these temperature fluctuations. Their effect on flow rate appears to have been minor, except for a somewhat greater effect in the flow/pressure ratio, as it will be discussed later.

Nucleate boiling at injector capillary was initiated as evidenced by the conditions of pressure and temperature achieved by the chamber after 10 minutes from initial point noted in Table 1.8. After this time, the power was increased slightly above the dryout limit, and smoother operation was obtained.

The most important information from the data sheet in Table 1.8 is presented in Figure 2.9 as relative flow degradation vs. time. The flow used in preparing this plot was first normalized by dividing it by the pressure difference between supply tank and steam line. The

pressure varied during the run due both to spontaneous drifts and slight downstream valve adjustments.

The quantity plotted is therefore

$$\text{Flow degradation} = 1 - \frac{(Q/\Delta P)}{(Q/\Delta P)_0}$$

Q = measured flow rate

$\Delta P = P_{Tank} - P_{Chamber}$

Figure 2.9 shows relatively wide fluctuations of flow degradation, but a fairly clear trend emerges after 60 - 80 minutes of continuous running.

At the end of the test that totalized 7.30 hours (total flow of 1.2 liters) a flow degradation of the order of 65 percent is apparent.

This experiment is a confirmation of the results of the report cited in reference 13 whose flow degradation curve is shown in Figure 2.1. The most important difference from that previous run was the slight adjustments of the downstream valve during the course of this subsequent run, trying to maintain the chamber pressure around five atmospheres. The results of this downstream value adjustment played an important role in the curve shape of Figure 2.9.

The flow rate was kept low compared with the previous run because in that test the chamber was powered with ten turns of heater wire and this one had only seven turns of the same heater wire around the chamber. So the flow rate was on purpose restricted at a low value by not making

adjustments in the upstream valve which was left in the same opening position from its initial value.

Finally, in Figure 2.10 one can see the blockage configuration obtained through a H-D Monopak Class 1 x-ray film observing the capillary injector. The smallest passage inside the capillary appears about 7 diameters from the upside end that was brazed to the conical end of the chamber. This confirms that the clogging appears within 5 to 10 diameters from the junction with chamber.

3.3 Calculation

Assuming there is still no deposition, then one can calculate the distribution of $\dot{q}(x)$, including boiling and vapor film effects.

One result of this calculation will be the location of the point of incipient boiling and the point of transition to film boiling (critical point). Given the vigorous generation of steam in the nucleate boiling, one would expect to find accumulation of NVR between these two points.

The following section presents such a calculation for the purpose of comparing to experimental results

The physical model assumed is based on a thermal analysis of the injector as in reference (6)

a - Heat conduction along stainless steel from near 800°K at tube end.

b - Negligible radiation loss.

c - Convection (laminar) in fluid up to boiling inception.

d - Boiling onset governed by surface tension.

e - Nucleate boiling up to boiling crisis.

f - Stable film boiling from crisis to head end.

(See the list of symbols on p. 7.)

Axial heat conduction along the wall:

$$Q_c = - K_w A_w \frac{dT_w}{dx} \tag{1}$$

$$\frac{dQ_c}{dx} = P_w \dot{q} \tag{2}$$

Forced convection:

$$Q_c = \dot{m}\, C_1 \frac{2}{3} F(T_w - T_b)\left(\frac{\delta}{r}\right)^2 \tag{3}$$

Combination of (1), (2) and (3) allows solutions for constant layer thickness (neglecting a short starting section where δ grows to its limit value).

$$\frac{\delta}{r} = \frac{2\left[\frac{K_w}{K_1} \frac{t_w}{r} \left(1 + \frac{t_w}{2r}\right)\right]^{1/5}}{\left(\frac{2}{3} FR_e P_r\right)^{2/5}} \tag{4}$$

$D_0 = 0.014$ in $= 3.556 \times 10^{-4}$ m (outside diameter)

$r_{inner} = 0.889 \times 10^{-4}$ m

at 80°C

$d_1 = 974.08$ kg/m^3

$C_{p_1} = 4196$ J/Kg°C

$\mu_1 = 354.6 \times 10^{-6}$ Nsec/m^2

$K_l = 0.668$ w/m°K

$\sigma = 0.063$ N/m

$P_r = 2.22$

$A_w = 7.445 \times 10^{-8} m^2$

$t_w = 0.889 \times 10^{-4} m$

at 600°K

$K_w = 20$ J/m sec°K

at 560°K

$d_v = 2.08$ Kg/m^3 (p=5 atm)

$K_v = 0.0422$ J/m sec°K

$C_v = 2026$ J/Kg°K

$R_g = 461$ J/Kg°K

$h_{fg} = 2.123 \times 10^6$ J/Kg

$C_{sf} = 0.013$ (SS304)(See list of symbols)

$g = 9.8$ m/sec^2

$T_{Laverage} = 824°K$

$P_{average} = 5.2$ atm

$T_{sat} = 423°K$

$T_b = 333°K$

Flow rate average = 2.9 cm^3/min

$u = 1.95$ m/sec

$\dot{m} = 0.468 \times 10^{-4}$ Kg/sec

$R_e = 952$

$F = 0.8$ (form factor, see reference (6))

Then, from equation (4)

$$\frac{\delta}{r} = 0.2574 \qquad \delta = 0.2288 \times 10^{-4} \text{m}$$

$$\dot{q}_{FC} = \frac{2K_l(T_w - T_b)}{\delta}$$

$$\dot{q}_{FC} = 5.839 \times 10^4 \ (T_w - 333) \ \text{w/m}^2 \tag{5}$$

Calculating $\dot{q}_{PB}$ from reference (6)

$$\dot{q}_{PB} = \mu_l h_{fg} \sqrt{\frac{(d_l - d_v)g}{\sigma}} \left[\frac{C_l}{h_{fg} C_{sf} P_r^{1.7}}\right]^3 (T_w - T_{sat})^3$$

$$\dot{q}_{PB} = 17.62(T_w - 423)^3 \ \text{w/m}^2$$

Onset of nucleate boiling using $\dot{q}$ minimum from reference (6)

$$\dot{q}_{ONB} = \frac{KPh_{fg}}{8R_g T_{sat}^2 \sigma} (T_w - T_{sat})^2$$

$$\dot{q}_{ONB} = 17969.13 \ (T_w - 423)^2 \tag{7}$$

Combination of equations (5) and (7) allows solution for

$$T_w = T_{ONB} = 441.8°\text{K}$$

$$\dot{q}_{ONB} = 6.351 \times 10^6 \ \text{w/m}^2$$

Then, using Rohsenow's method for nucleate boiling

$$\dot{q}_{NB} = \dot{q}_{FC} + \dot{q}_{PB} - \dot{q}_{PB(ONB)}$$

$$\dot{q}_{NB} = 5.839\times10^{4}(T_w-333) + 17.62(T_w-423)^3 - 1.171\times10^{5} \qquad (8)$$

$$\dot{q}_{NB} = 0 \qquad \text{at } T_w=372.9°K$$

Film Boiling: assume stable film using Bromley's correlation (radiation component negligible (17))

$$\dot{q}_{FB} = 2.7\sqrt{\frac{uK_v d_v}{2r}\,[h_{fg}+0.4C_{p_v}(T_w-T_{sat})](T_w-T_{sat})}$$

$$\dot{q}_{FB} = 2384.8\,\sqrt{2619.7(T_w-423)+(T_w-423)^2} \qquad (9)$$

negligible

Critical heat flux: using CISE correlation from reference (6)

$$\dot{q}_{cr} = \frac{\dot{m}[\alpha h_{fg}+C_l(T_{sat}-T_b)]}{P_w L\left(1+\frac{\beta D_i}{L}\right)}$$

where

$$\alpha = \frac{1-P/P_{cr}}{1.11(G/10^6)^{1/3}}\,; \qquad \alpha \leq 1$$

$$\alpha = 0.788$$

$$\beta = 62\left(\frac{P_{cr}}{P}-1\right)^{0.4}\left(2r_i\right)^{0.4}\left(\frac{G}{10^6}\right) = 52.3$$

r_i in inches

D_i in ft

L in ft

P_w in ft

h_{fg} in BTU/lb

C_l in BTU/lb°F

G in BTU/lb ft^2

$\dot{m}$ in lb/hr

T in °F

$\dot{q}_{cr}$ in BTU/hr ft^2

$$\dot{q}_{cr} = 4.7848 \times 10^6 \text{ BTU/hr ft}^2$$

$$\dot{q}_{cr} = 1.511 \times 10^7 \text{ w/m}^2 \tag{10}$$

The wall temperature calculation from (1) and (2)

$$\frac{dT_w}{dx} = -\sqrt{\frac{4r}{K_w t_w (2r+t_w)}} \sqrt{\int_{T_b}^{T_w} \dot{q} dT_w}$$

$$\frac{dT_w}{dx} = -27.3844 \sqrt{\int_{T_b}^{T_w} \dot{q} dT_w} \tag{11}$$

which can be calculated one $\dot{q}(T_w)$ is known in the different regimes.

Forced convection from equation

$$\int_{333}^{T_w} 58390(T_w-333)dT_w = 29195(T_w-333)^2$$

$$-\left[\frac{dT_w}{dx}\right]_{FC} = 4679(T_w-333)$$

which integrates to

$$T_w = 333 + 108.8 \exp[-4679(X-X_{ONB})] \tag{12}$$

$$\text{at } X \geq X_{ONB}$$

Nucleate boiling from equation (8)

$$\int_{372.9}^{T_w} \dot{q}_{NB} dT_w = \int_{372.9}^{T_w} [58390(T_w-333)+17.62(T_w-423)^3-1.171\times10^5]dT_w$$

$$\theta = \int_{372.9}^{T_w} \dot{q}_{NB} dT_w = 29195[(T_w-333)^2-1592]+4.405[(T_w-423)^4-6.3\times10^6] - 1.171\times10^5(T_w-372.9)$$

Then, defining $f(T_w) = 27.3844\sqrt{\theta}$

$$-\left[\frac{dT_w}{dx}\right]_{NB} = f(T_w)$$

$$X = X_{ONB} - \int_{441.8}^{T_w} \frac{dT_w}{f(T_w)}$$

or

$$X = X_{ONB} - F(T_w);\ \dot{q} = \dot{q}_{NB}(X)$$

In particular, when $\dot{q} = \dot{q}_{cr}$, $T_w = T_{cr}$

$$X_{cr} = X_{ONB} - F(T_{cr})$$

$$T_{cr} = 492.4$$

From equation (8), where $\dot{q}_{NB} = \dot{q}_{cr}$

$$F(T_{cr}) = \int_{441.8}^{492.4} \frac{dT_w}{f(T_w)} = 0.0000878$$

by Simpson's approximation.

Intermediate values

T_w(°K)	441.8	445	450	455	460
$F(T_w)$	0	0.0706×10^{-4}	0.176×10^{-4}	0.275×10^{-4}	0.370×10^{-4}

T_w(°K)	465	470	475	480	485
$F(T_w)$	0.459×10^{-4}	0.544×10^{-4}	0.625×10^{-4}	0.702×10^{-4}	0.776×10^{-4}

T_w(°K)	490	492.4
$F(T_w)$	0.845×10^{-4}	0.878×10^{-4}

Then,

$$X_{cr} = X_{ONB} - 0.0000878 \tag{13}$$

For the boiling film region from equation (9)

$$\int_{423}^{T_w} \dot{q}_{FB} dT_w = \int_{423}^{T_w} 1.2206 \times 10^5 (T_w - 423)^{1/2} dT_w = 81373.3 (T_w - 423)^{3/2}$$

From equation (11)

$$\frac{dT_w}{(T_w - 423)^{3/4}} = - 7811.7 dx$$

$$4(T_w - 423)^{1/4} = - 7811.7x + \text{Const.}$$

$$4(T_{cr} - 423)^{1/4} = - 7811.7x_{cr} + \text{Const.}$$

Substituting X_{cr} from equation (13)

$$4[(T_w-423)^{1/4}-(T_{cr}-423)^{1/4}] = 7811.7(x_{ONB}-0.0000878-x) \qquad (14)$$

In particular in equation (14) when

$$T_w = T_0 \qquad x = 0$$

(T_0 = temperature of capillary-chamber junction)

$$(T_0-423)^{1/4} = 2.7148 + 1952.93\ x_{ONB} \qquad (15)$$

Next the value of T_0 will be estimated

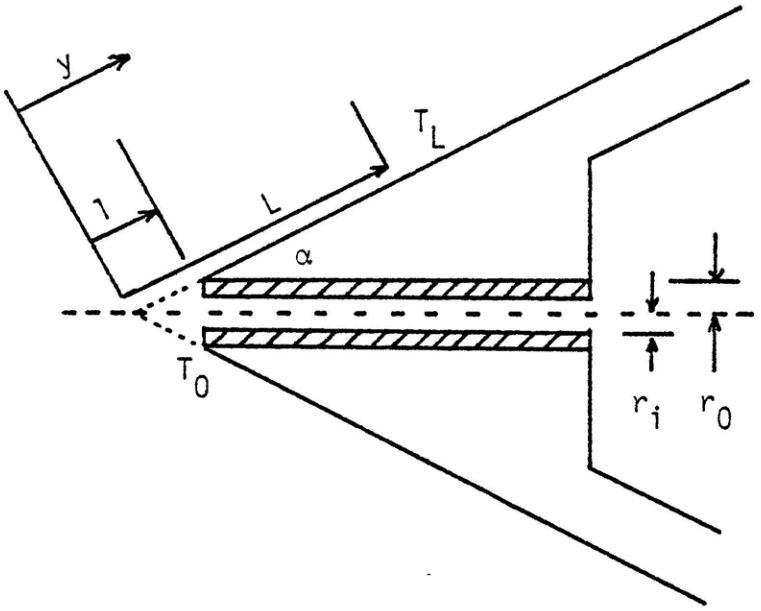

$r_i = 0.889 \times 10^{-4}$ m

$\sin\alpha = 0.5299$

L = 0.001 m

T_0 = Temperature of capillary-chamber junction

T_L = Temperature at point where it was brazed with the thermocouple

$$l = \frac{r_0}{\sin \alpha} = 0.00034 \text{ m}$$

Notice that $l \sin\alpha - r = t_w$

$$(\pi y^2 \sin^2\alpha - \pi r_i^2) K_w \frac{dT_w}{dy} = Q$$

$$T_0 = T_L + \frac{Q}{K_w} \left[\frac{1}{2\sqrt{\pi \sin^2\alpha (\pi r_i^2)}} \ln \frac{y\sqrt{\pi \sin^2\alpha} \quad \sqrt{\pi r_i^2}}{y\sqrt{\pi \sin^2\alpha} + \sqrt{\pi r_i^2}} \right]_L^l$$

Then

$$T_0 = T_L - 125.4Q \tag{16}$$

$$Q = 2\pi r \left[\int_{X_{ONB}}^{\infty} \dot{q}_{FC} dx + \int_{X_{cr}}^{X_{ONB}} \dot{q}_{NB} dx + \int_0^{X_{cr}} \dot{q}_{FB} dx \right] \tag{17}$$

From equations (5) and (12)

$$\dot{q}_{FC} = 58390 \cdot 108.8 \exp[-4679(X - X_{ONB})]$$

$$\int_{X_{ONB}}^{\infty} \dot{q}_{FC} dx = 1357.73 \text{ w/m}$$

From equation 181; repeated here

$$\dot{q}_{NB} = 58390(T_w-333) + 17.62(T_w-423)^3 - 1.171\times10^5$$

$$X = X_{ONB} - F(T_w)$$

Integrating numerically by rectangular approximation, observing the intermediate $F(T_w)$ values, already calculated and using a $\dot{q}_{NB}$ average for each subinterval

T_w(°K)	X	$\Delta X\cdot\dot{q}_{NB}$
441.8	$X_1 = X_{ONB}$	
445	$X_2 = X_{ONB}-0.0706\times10^{-4}$	45.76
450	$X_3 = X_{ONB}-0.176\times10^{-4}$	72.05
455	$X_4 = X_{ONB}-0.275\times10^{-4}$	72.49
460	$X_5 = X_{ONB}-0.370\times10^{-4}$	74.93
465	$X_6 = X_{ONB}-0.459\times10^{-4}$	76.04
470	$X_7 = X_{ONB}-0.544\times10^{-4}$	79.08
475	$X_8 = X_{ONB}-0.625\times10^{-4}$	82.47
480	$X_9 = X_{ONB}-0.702\times10^{-4}$	86.16
485	$X_{10} = X_{ONB}-0.776\times10^{-4}$	91.34
490	$X_{11} = X_{ONB}-0.845\times10^{-4}$	94.21
492.4	$X_{12} = X_{ONB}-0.878\times10^{-4}$	48.55

Then

$$\Sigma\Delta X\cdot\dot{q}_{NB} = 823.08$$

From equations (13) and (14)

$$(T_w-423)^{1/4} = 2.886 + 1952.93(X_{cr}-X)$$

$$\dot{q}_{FB} = 1.2206\times10^5\sqrt{(T_w-423)} = 1.2206\times10^5[2.886+1952.93(X_{cr}-X)]^2$$

Integrating

$$\int_0^{X_{cr}} \dot{q}_{FB}dx = 20.83[2.886+1952.93X_{cr}]^3 - 500.7$$

From equation (17)

$$Q = 2\pi\cdot0.889\times10^{-4}[1357.73+823.08+20.83[2.886+1952.93X_{cr}]^3 -500.7]$$

$$Q = 0.938 + 0.0116(2.886+1952.93X_{cr})^3$$

From equation (16)

$$T_0 = 824 - 125.4[0.938+0.0116(2.886+1952.93X_{cr})^3] \qquad (18)$$

Then plotting equations (15) and (18) in Figure 2.11, one can find

$$X_{ONB} = 0.000550 \text{ m}$$

$$T_0 = 627°K$$

Thus, the results of the calculation indicate a prediction of nucleate boiling between 0.550 mm and 0.462 mm from the tube attachment to the chamber. This is the region where NVR deposition can be expected, and, in fact, one can expect deposition rate to be proportional to the local value of $\dot{q}(x)$ (at least in the initial phase of the process),

therefore peaking near the critical point (0.462 mm from the chamber). These results are compared to the experimental data in the next chapter.

Chapter 4

CONCLUSIONS AND RECOMMENDATIONS

The calculation in Section 3.3 showed that, for the conditions as used in this experimental work, the onset boiling point inside the capillary injector would be about 3 diameters from the conical end of the chamber. This agrees with previous study (6) at MIT that estimated, for this non volatile residue simulation experiment, the moving of the boiling region closer to the tube hot end and agrees also with Figure 2.10 where two major boiling regions appear to have occurred at about 3 diameters (arrow a) and about 7 diameters (arrow b) from the upper end of the tube.

The presence of two separated deposition regions could possibly be explained by the two different operating conditions for the first two hours of the test versus the remainder of the same test. The calculations in Section 3.3 were for an average value of the data from Table 1.8, and resulted in a predicted location, of the deposition region, just 3 diameters from the upper end of the tube. From more detailed calculations, reported in reference (6), one can estimate a shift of X_{ONB} by 4 diameters for pressure chamber changing from 100 psi to 75 psi, which were the pressures prevailing an average during these two periods.

On closer examination, the tube region between 3 and 7 diameters is seen in the X-ray picture (Figure 2.10) to have a reduced diameter

suggesting additional calcium sulfate deposition in this area. This could be understood as a consequence of the operating procedures followed during the run. After the initial two hours, when deposition had already reduced the flow passage somewhat (presumably at the 3 diameter location), the chamber pressure showed a tendency to increase spontaneously, probably due to the decreasing of the flow with the time and due to a somewhat erratic downstream valve performance in the two-phase flow. This variable chamber pressure was normalized out of the data on flow degradation (Figure 2.9). However, in order to maintain a chamber pressure of about 75 psia periodic adjustments were made to this downstream value. It is hypothesized that these pressure excursions, which entailed corresponding excursions of the saturation temperature, produced a back-and-forth motion of the onset boiling point, although still with most of the deposition occurring at about 7 diameters, corresponding to predominant dwell at 75 psia.

Clearly, more detailed experimentation would be required to substantiate these conclusions.

Another important consideration in these conclusions would be about the temperature distribution along the capillary. By the calculation in Section 3.3 one can understand that integration limits play an important role in the theoretical exact position of the onset boiling point inside the tube. Those limits on the temperature distribution in Figure 2.12 still need a confirmation of what can be obtained in further research using, for example, brazed small thermocouples along the capillary injector wall.

It is also recommended that alternative techniques for examination of the tube after a test be investigated in order to improve the resolution.

Finally, we will list a summary of relevant considerations for future work in this area (15).

a. Determination of similarities and differences between water and hydrazine data will clarify the issue of physical versus chemical effects.

b. Indications of boiling as deposition mechanism seem clear; but other effects, including chemistry can not be ruled out.

c. Correlation of deposition pattern with heat flow calculations for the different running conditions will establish validity of analytical tool in analyzing new concepts.

d. The tube injector type should be designed to maintain always the liquid temperature in the region near the chamber conical end above the temperature of the onset boiling point for the used line pressure. This condition is not met by the feed tube design for liquid propellant as shown in Figure 2.13.

REFERENCES

1. D.E. Fritz, R.L. Sackheim, J.C. Lewis, "Understanding Flow Blockage in Small Thrusters," Redondo Beach, California 90278.

2. Russi, M.J., "A Survey of Monopropellant Hydrazine Thruster Technology," AIAA/SAE 9th Propulsion Conference, AIAA Paper No. 73-1263, November 1973.

3. Zafran, S. et al, "Flight Applications of High Performance Electrothermal Thrusters," AIAA Paper No. 77-965, AIAA/SAE 13th Joint Propulsion Conference, Orlando, Florida, July 1977.

4. Pugmire, T.K., Macklis, H. and Sackhein, R.L., "Application of Power Augmented Hydrazine Thrusters," AIAA Paper No. 78-1065, AIAA/SAE 14th Joint Propulsion Conference, Las Vegas, Nevada, July 1978.

5. Martinez-Sanchez, M., Class Notes of Subject 16.531, "Space Propulsion and Power Generation," Cambridge, MA, MIT, 1982.

6. Martinez-Sanchez, M., "First Progress Report on P.O. SP605448-AM Ford Aerospace Contract," Cambridge, MA, MIT, May 30, 1979.

7. Schereib, R., "Flow Anomalies in Small Hydrazine Thrusters," AIAA Paper No. 79-1303, AIAA/SAE/ASME 15th Joint Propulsion Conference, Las Vegas, Nevada, June 18-20, 1979.

8. Ellion, M.E. et al, "Development of a Long life 0.2 lbf Heaterless Thruster Without Pulse Mode Degradation," AIAA Paper No. 78-1063, AIAA/SAE 14th Joint Propulsion Conference, Las Vegas, Nevada, July 1978.

9. JPL Interoffice Memo 358:73:321, "Microthruster Capillary Examination (Hot Gas Attitude Control for MJS-77)," March 27, 1973.

10. "Mariner Jupiter/Saturn LCSSE Thruster Valve Assembly Technical Manual, Maintenance and Service Instructions," Rocket Research Corporation, RRC Document No. EP-0018, Rev. B, May 25, 1976.

11. Fritz, D.E. and Kwan, M., TRW Company Correspondence, "RRC 0.2 lbf Thruster Disassembly and Results," June 12, 1978.

12. Schreib, R.R., "ATS-6 Propulsion Performance: Four Years in Orbit," AIAA/SAE 14th Joint Propulsion Conference AIAA Paper No. 78-1062, Las Vegas, Nevada, July 25-27, 1978.

13. Martinez-Sanchez, M., "Water Simulation Test," Report to Ford Aerospace and Communications Corp., Cambridge, MA, MIT, July 9, 1980.

14. Martinez-Sanchez, M., "Proposal for No-Cost Extension of Research on Satellite Thruster Feed System," submitted to Ford Aerospace and Communications Corp., Cambridge, MA, February 1, 1980.

15. Martinez-Sanchez, M., "Progress Report to Ford Aerospace and Communication Corp.," Cambridge, MA, MIT, December 14, 1979.

16. Seidell, A., Linke, W.F., "Solubilities of Inorganic and Metal-Organic Compounds," D. Van Nostrand Co., Inc., Princeton, NJ, 1958.

17. Wong, H.Y., "Heat Transfer for Engineers," First edition 1977, Longman, New York, p. 136.

18. Rohsenow, W.M., Hartnett, J.P., "Handbook of Heat Transfer," McGraw-Hill, Inc., 1973.

Table 1.1 Some Flight Applications of 0.1 to 0.2 lbf Hydrazine Thrusters (From reference (1))

Program	Nominal Thrust Level, LBF	Manufacturer Thruster	Main Use	Prime/User
ATS-6	0.1	RRC	Attitude Control & ΔV	Fairchild NASA/GSFC
SOLRAD SERIES	0.2	HAM STD	Attitude Control	NRL
IUE	0.2	HAM STD	Attitude Control & ΔV	NASA/GSFC
SATCOM	0.2	RRC	Attitude Control & ΔV	RCA
CTS	0.2	HAM STD	Attitude Control & ΔV	Canadian Gov't
GPS (NAVSTAR)	0.2	RRC	Attitude Control & ΔV	R.I./SAMSO
MJS-77 (VOYAGER)	0.2	RRC	Attitude Control & TCM	NASA/JPL
FLTSATCOM	0.2	TRW	Attitude Control	TRW/SAMSO
OTS/MAROTS	0.2	ERNO/TRW	Attitude Control & ΔV	ERNO/ESA
ETS-III	0.2	IHI/TRW	Attitude Control & ΔV	Toshiba/ Japan
BSE	0.2	HAM STD	Attitude Control & ΔV	G.E./Japan
ANIK B	0.2	RRC	Attitude Control & ΔV	RCA/Canada
TIP II	0.2	HAM STD	Zero Reaction Venting	RCA/APL
INTELSAT V	0.2	RRC	Attitude Control	Ford ACC/ INTELSAT
INTELSAT V	0.1 (HIPEHT)	TRW	N.-S. ΔV	Ford ACC/ INTELSAT
MMS	0.1	Hughes	Attitude Control	Fairchild NASA/GSFC

Table 1.2 Comparison of Hydrazine Grades
(From reference (1))

Constituents	Requirements: MIL-P-26536 Standard Grade	Requirements: MIL-P-26536 Monopropellant Grade	Requirements: Purified Hydrazine VI.C Grade	Requirements: Purified Hydrazine VGR 77 Grade	Ultra-Pure Hydrazine (Capability)	TRW[1] Sampling Results for VLC Grade Hydrazine
Hydrazine (% by wt)	98.0 min	98.5 min	98.0 min	98.5 min	99.3 min	Not performed
Chloride (% by wt)	n/c[2]	0.0005 max	n/c	0.0005 max	0.0001[3] max	Not performed
Aniline (% by wt)	n/c	0.5 max	0.008 max	0.005 max	0.002[3] max	Not performed
Iron (% by wt)	n/c	0.002 max	n/c	0.002 max	0.0002[3] max	0.075-0.25 (ppm, mg/l)
CO_2 (% by wt)	n/c	0.02 max	n/c	0.005 max	0.0005[3] max	Not performed
Water (% by wt)	1.5 max	1.0 max	0.5-1.5	0.5-1.0	0.2 max	Not performed
Particulate (mg/l)	10.0 max	1.0 max	10.0 max	1.0 max	1.0[3] max	Not performed
Other volatile carbonaceous material (% by wt)	n/c	0.02 max	n/c	0.02 max	0.01[3] max	Not performed
Ammonia (% by wt)	n/c	n/c	0.4 max	0.4 max	0.4 max	Not performed
NVR (% by wt)	n/c	0.005 max	0.003 max	0.005 max	0.0005[3] max	
Calcium (ppm, mg/l)	n/c	n/c	n/c	n/c	n/c	0.052-0.323
Nickel (ppm, mg/l)	n/c	n/c	n/c	n/c	n/c	0.101-0.380
Chromium (ppm, mg/l)	n/c	n/c	n/c	n/c	n/c	0.016-0.082

(1) Range of 8 samples as withdrawn from propellant drums and from the TRW test stand. Estimated accuracy is ±5% for atomic absorption spectroscopy.

(2) n/c means not controlled.

(3) Capability controlled by analysis accuracy.

Table 1.3 Thrust Degradation During Mission or Ground Life Test Caused by Injector Tube Flow Blockage (From reference (1))

Program	Nominal Thrust Level (lb_f)	Data Source	Flow Reduction (Percent)	Firing Mode/ Throughput	NVR Constituents	Tank Elastomer	Ref.
JPL/TOPS	0.1	Evaluation test for hot gas attitude control	100 (3rd flow blockage)	Varying duty cycles, 1400 hrs firing time	Fe, K, Ca	No	6
VCR-LOSSE TVA Development	0.2	Life margin tests	27	S.S./156 lb	Fe, Sr, other	No	7
HiPHET	0.1	Development and qual tests	20	S.S./180 lb	Ca, Fe, Al, K	No	-
Voyager 1977	0.2	Extended life qual tests	45	S.S./160 lb Pulse/53 lb	Ca, Fe, Al, K Nitrides	Yes AFE-332	8
MMS	0.2	Development test	100	Pulse/30 lb	Ca, other	No	5
ATS-6	0.2	Orbit performance	100	S.S. & Pulse	?	Yes EPT-10	9

Table 1.4 Water and Hydrazine Properties

	Water	Hydrazine
Vapor Pressure (25°C)	23.756 mm	14.38 mm
Density, Liquid	1.000 g/cc	1.0045 g/cc
Freezing Point	0.00°C	1.5°C
Boiling Point	100.0°C	113.5°C
Surface Tension	72.14 dynes/cm	66.67 dynes/cm
Viscosity, Liquid	0.89 centipoise	0.90 centipoise
Heat of Vaporization	9.717 kcal/mole	9.600 kcal/mole
Specific Heat	0.999 cal/g°C	0.720 cal/g°C
Critical Temperature	374.2°C	380°C
Critical Pressure	218.3 atm	145 atm
Critical Density	0.325 g/cc	0.231 g/cc

Table 1.5 Heater Wire Specifications

Sheath		Wire		Insulation			
Diameter Inch	Material	Diameter Inch	Material	Resistivity M -ft	Material	Continuity Resistance	Max Rec Volt
.040	Stainless Steel	.006	Nichrome	1000 Ω	MgO	16.3	85
.060	Stainless Steel	.010	Nichrome	1000 Ω	MgO	6.5	115
.063	Stainless Steel	.010	Nichrome	1000 Ω	MgO	6.5	115
.080	Stainless Steel	.013	Nichrome	1000 Ω	MgO	3.9	180

Table 1.6 Thermocouple Specifications
Iron-Constantan (Ansi Symbol J)

Useful Range	-300 to 1600°F
EMF	-7.52 to 50.05 mV
Constantan Composition	55% Cu - 45% Ni
Constantan Melting Point	1270°C
Constantan Density	8.86 g/cm^3
Constantan	Non-Magnetic, Negative (-)
Iron Purity	99.9%
Iron Melting Point	1536°C
Iron Density	7.9 g/cm^3
Iron	Magnetic - Positive (+)

Table 1.7 Capillary Specifications
Stainless Steel Tube Type 304,
18-8 Austenitic (Hard Temper)

Standard Gages and Tolerances

Gage	OD	OD Tolerance	Nominal Wall	Wall Tolerance
27	.016"	+.0005" -.000"	.00425"	+.000" -.0005"
28	.014"	+.0005" -.0000"	.0035"	±.00025"
29	.013"	+.0005" -.0000"	.003"	±.00025"
30	.012"	+.0005" -.0000"	.003"	±.00025"

Table 1.8 Data from Test

Time		Flow Rate	Pressure (psi)		Temperature	Supply	
hr	min	cc/min	Tank	Chamber	mV	Volts	cc/mm/Δp
0	0	7.0	150	65	10.0	21.0	0.0824
	10	3.5	150	105	26.2	22.0	0.0778
	20	5.0	150	90	26.2	22.0	0.0833
	30	4.0	150	100	27.9	22.4	0.0800
	40	4.5	170	95	28.0	22.8	0.0600
	50	3.5	150	105	29.4	22.8	0.0778
1	60	4.0	165	110	28.3	22.8	0.0730
	70	3.6	155	108	28.8	22.8	0.0770
	80	4.0	150	95	27.2	22.8	0.0730
	90	5.0	145	35	22.5	20.0	0.0453
	100	3.0	130	79	25.5	20.0	0.0588
	110	3.2	150	70	29.6	21.8	0.0400
2	120	3.0	147	80	29.8	21.8	0.0448
	130	2.7	145	82	30.0	21.8	0.0428
	140	2.9	143	75	30.1	21.8	0.0427
	150	2.7	140	78	30.6	21.8	0.0435
	160	2.7	157	75	30.7	21.8	0.0328
	170	2.6	153	85	30.6	21.8	0.0383
3	180	2.7	145	70	31.0	21.8	0.0360
	190	2.5	147	78	31.4	21.8	0.0362
	200	2.9	143	65	31.5	21.8	0.0372
	210	2.6	143	70	31.5	21.8	0.0357
	220	2.5	140	70	31.6	21.8	0.0357
	230	2.3	147	72	32.6	21.8	0.0307
4	240	2.7	155	70	32.3	21.8	0.0320
	250	2.7	155	70	32.3	21.8	0.0320
	260	2.6	150	69	29.5	22.2	0.0321
	270	2.4	147	79	29.7	22.2	0.0353
	280	2.5	145	87	29.7	22.2	0.0431
	290	2.5	144	79	29.1	22.2	0.0385
5	300	2.4	143	78	28.7	22.2	0.0369
	310	2.4	140	76	29.3	22.2	0.0375
	320	2.3	143	77	29.2	22.2	0.0348
	330	2.7	157	73	29.3	22.2	0.0321
	340	2.6	155	82	28.6	22.2	0.0356
	350	2.5	154	87	28.3	22.2	0.0373

Table 1.8 (Continued)

Time		Flow Rate	Pressure (psi)		Temperature	Supply	
hr	min	cc/min	Tank	Chamber	mV	Volts	cc/mm/Δp
6	360	2.3	152	87	28.3	22.2	0.0354
	370	2.3	150	87	28.7	22.2	0.0365
	380	2.2	150	85	28.6	22.2	0.0338
	390	2.3	147	79	29.3	22.2	0.0338
	400	2.2	146	85	29.0	22.2	0.0361
	410	2.1	145	84	30.2	22.2	0.0344
7	420	2.0	145	84	29.8	22.2	0.0328
	430	2.2	150	87	28.8	22.2	0.0349
	440	2.1	150	85	29.6	22.2	0.0323
	450	2.0	148	79	30.3	23.0	0.0290
	460	1.5	142	91	32.9	23.0	0.0294

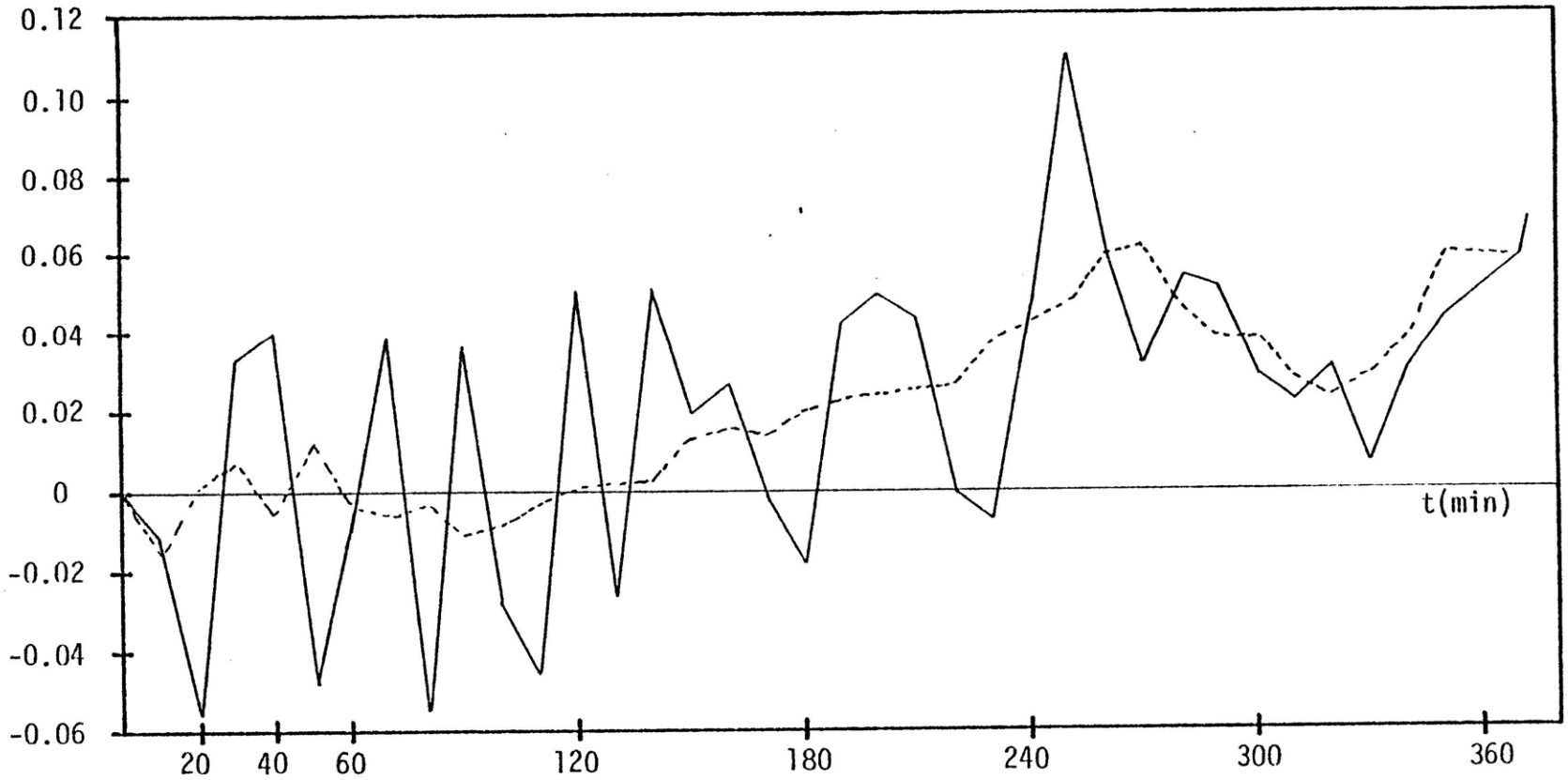

Figure 2.1 Relative flow degradation versus run time.
The dotted line is a 5-point average of the data.
(From reference (6))

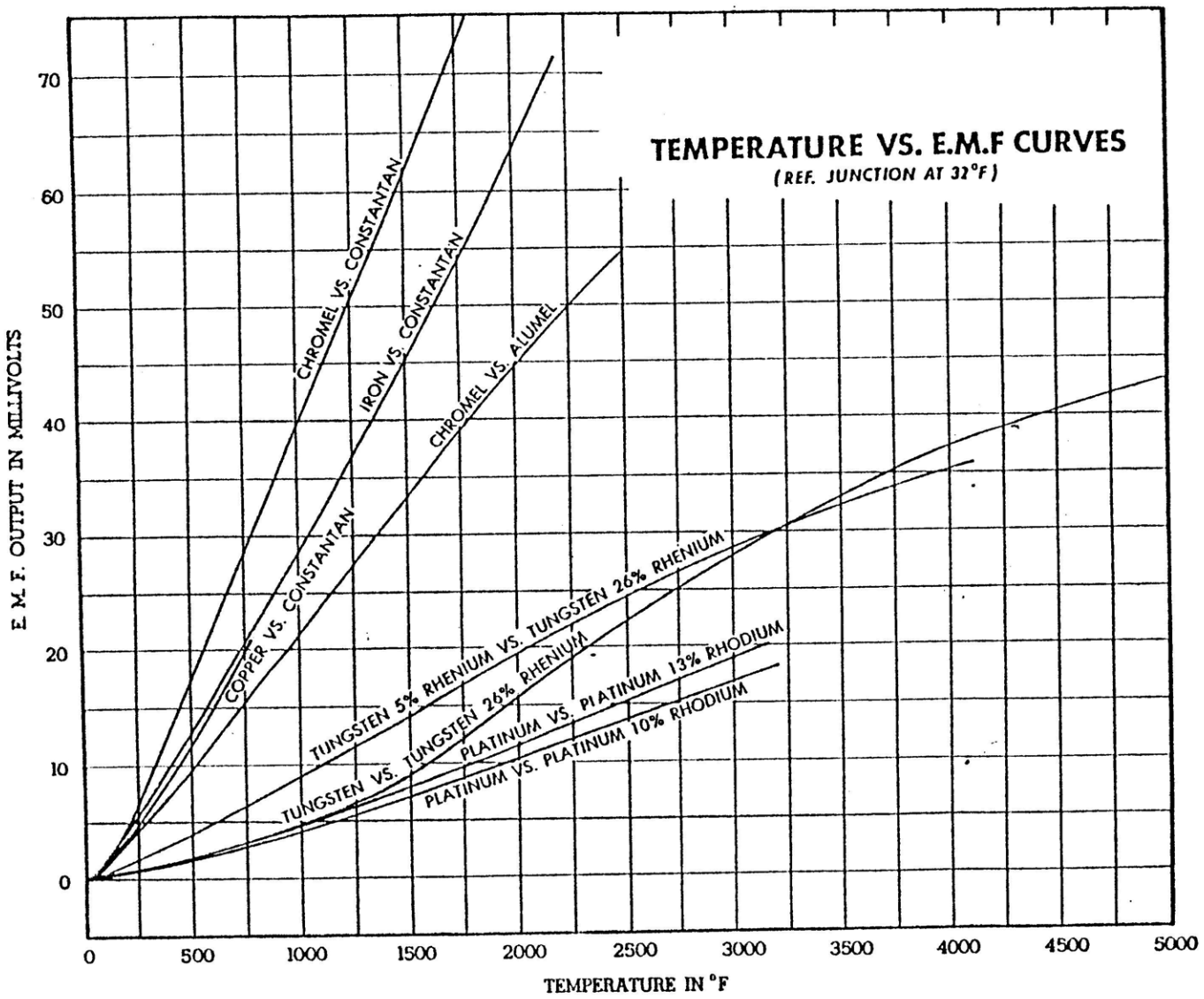

Figure 2.2 Temperature-Millivolt Graph for Thermocouples.

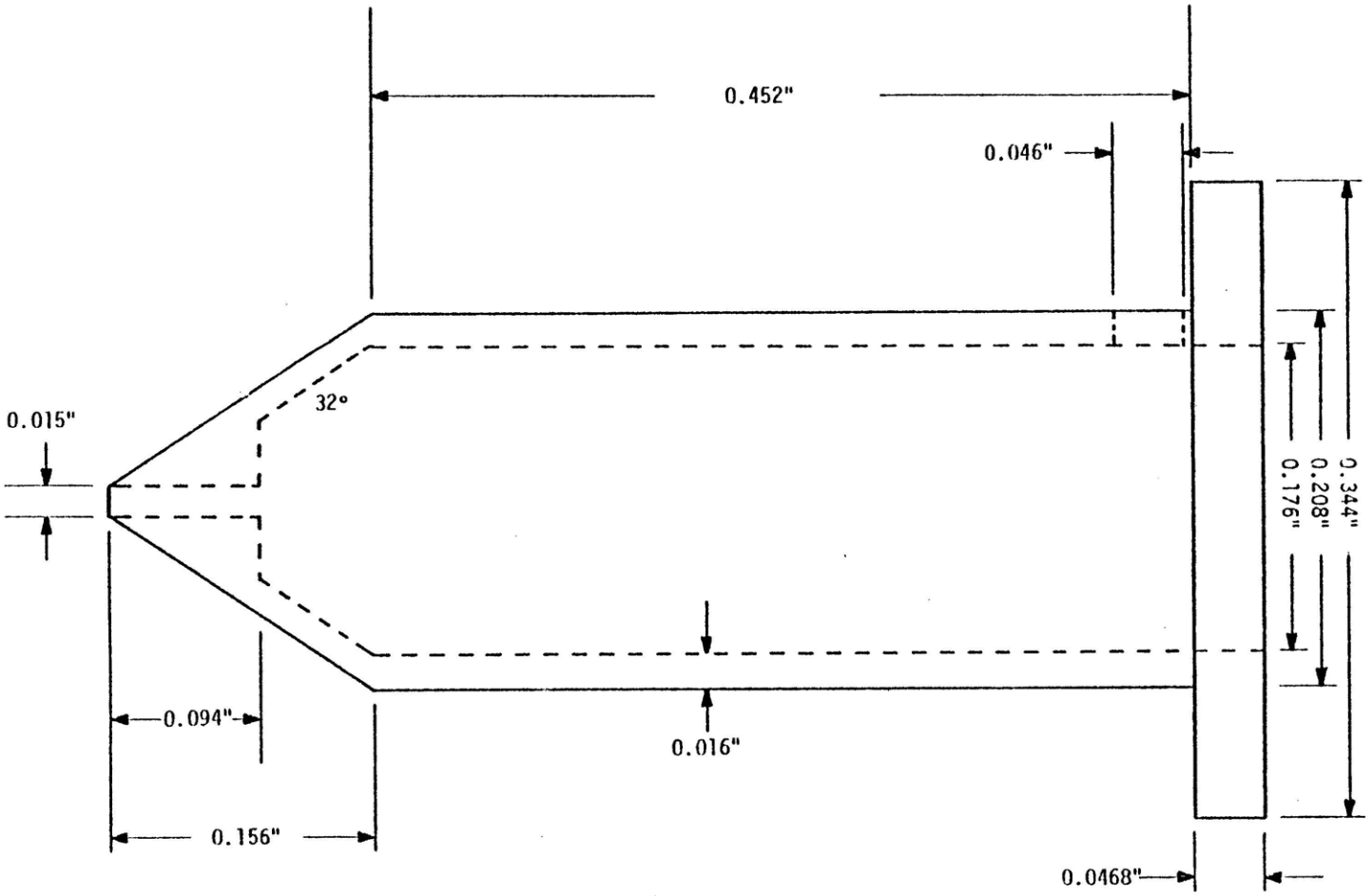

Figure 2.3 Chamber Design

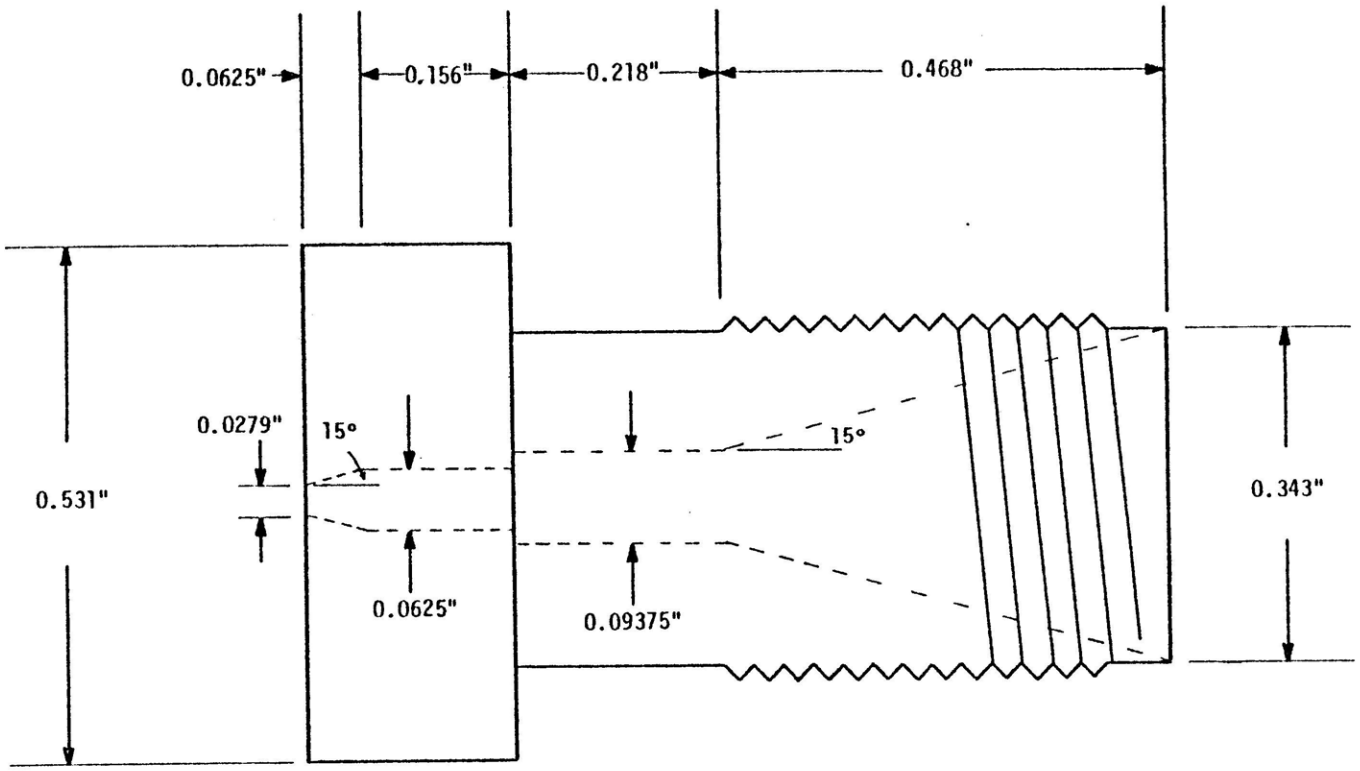

Figure 2.4 Exhaust Nozzle Design

1) Nitrogen Tank
2) Nitrogen Pressure Gauge
3) Water Tank
4) Water Tank Pressure Gauge
5) Upstream Valve
6) 60 Microfilter
7) Flowmeter

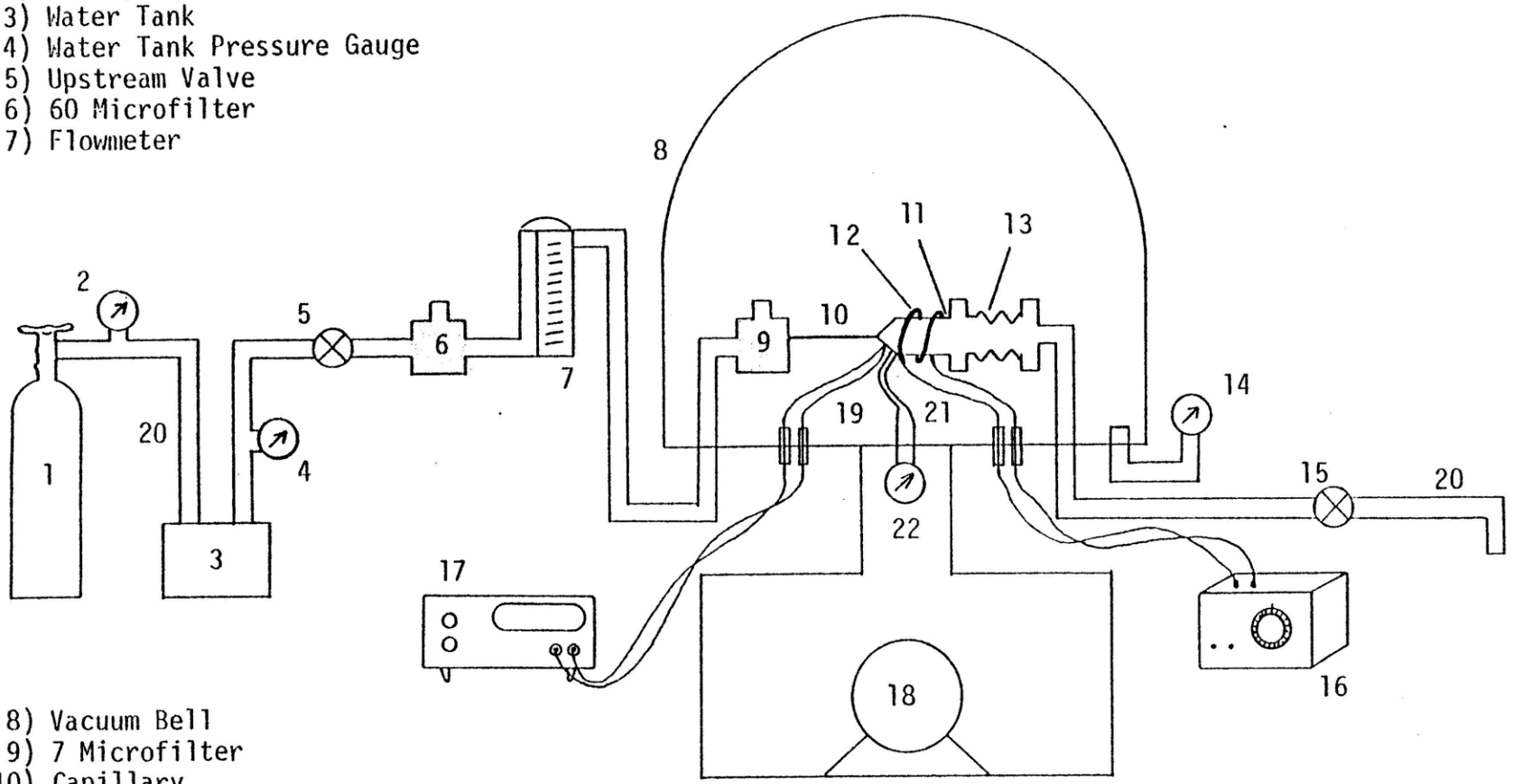

8) Vacuum Bell
9) 7 Microfilter
10) Capillary
11) Chamber
12) Heater Wire
13) Nozzle
14) Vacuum Gauge
15) Downstream Valve
16) Transformer
17) Multitester
18) Vacuum Pump
19) Thermocouple
20) Copper Tube
21) Copper Wire
22) Pressure Chamber Gauge

Figure 2.5 Schematic of Instrumentation and Equipment

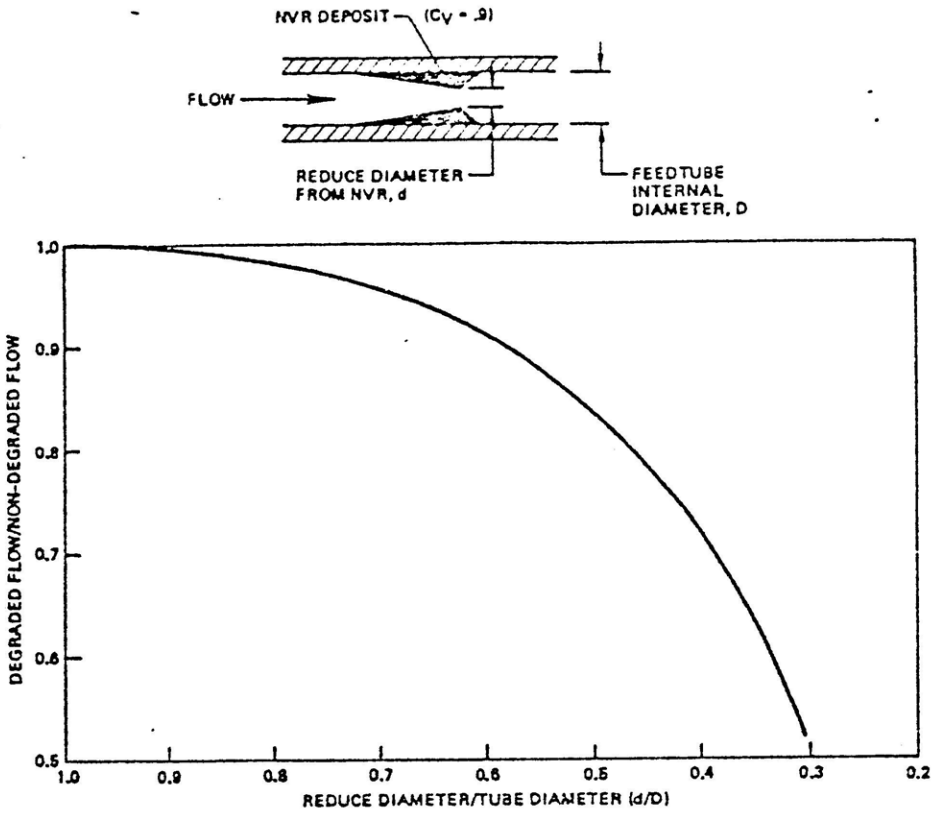

Figure 2.6 Flow Degradation vs. Feedtube Diameter Reduction (From reference (1))

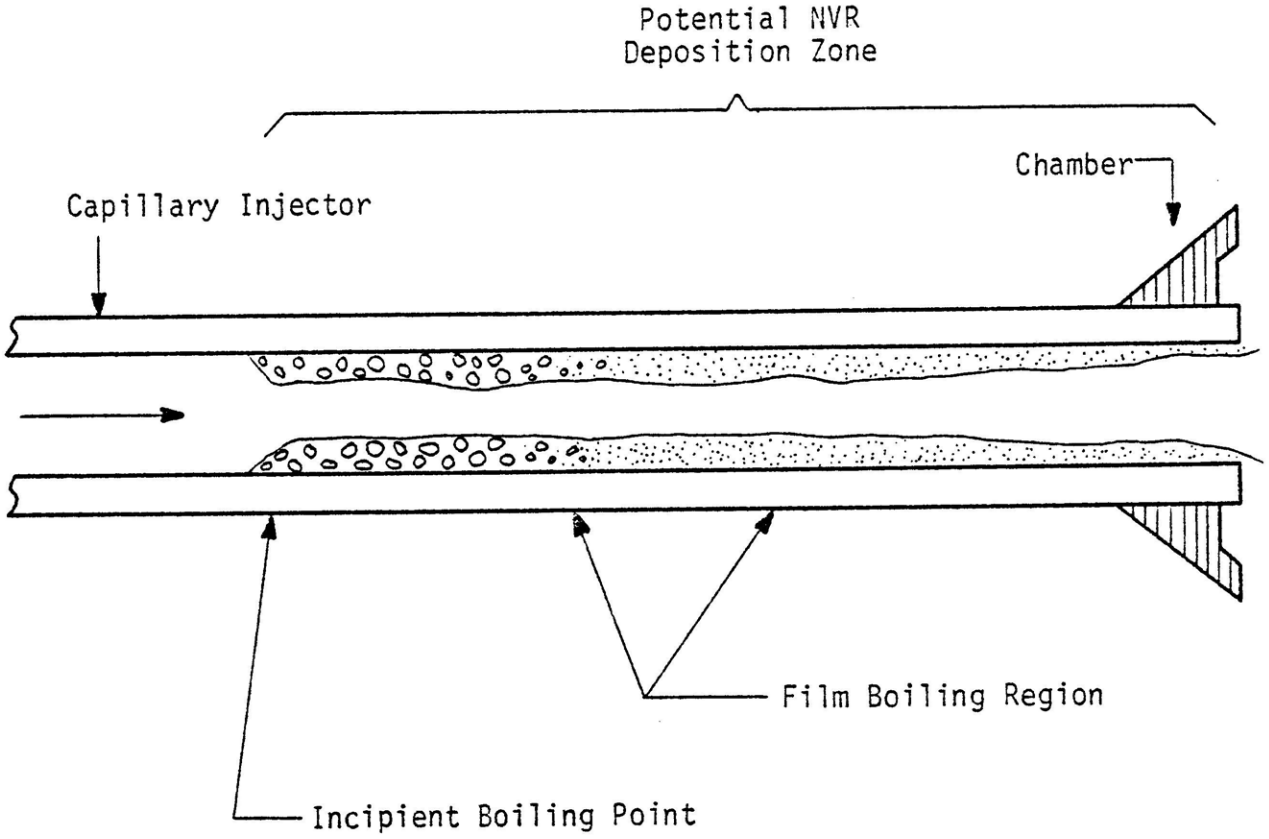

Figure 2.7 Potential Mechanism for NVR Deposition

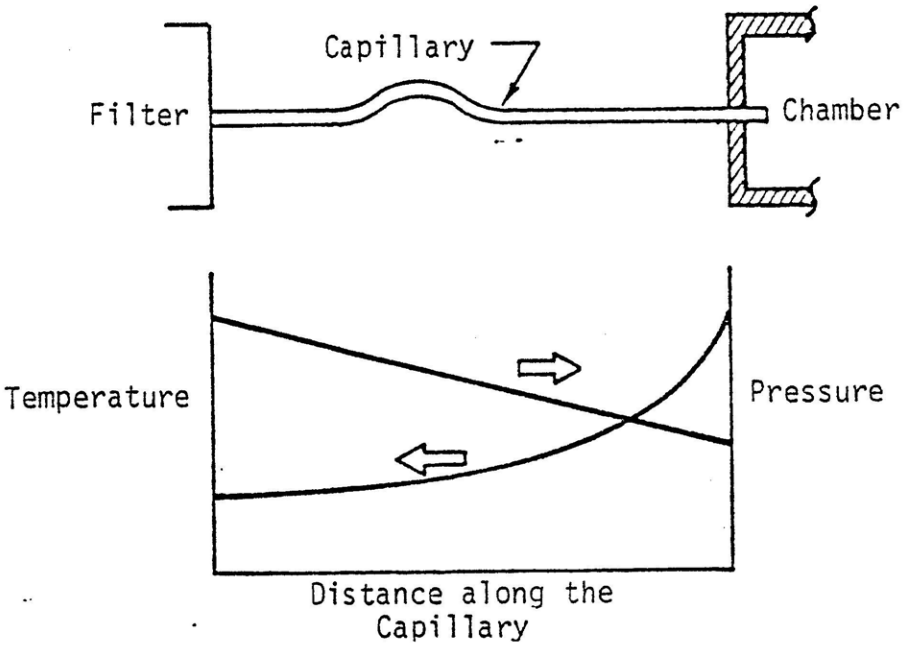

Figure 2.8 Feed Tube Pressure and Temperature Characteristics

Figure 2.9 The Relative Flow Degradation in the Test

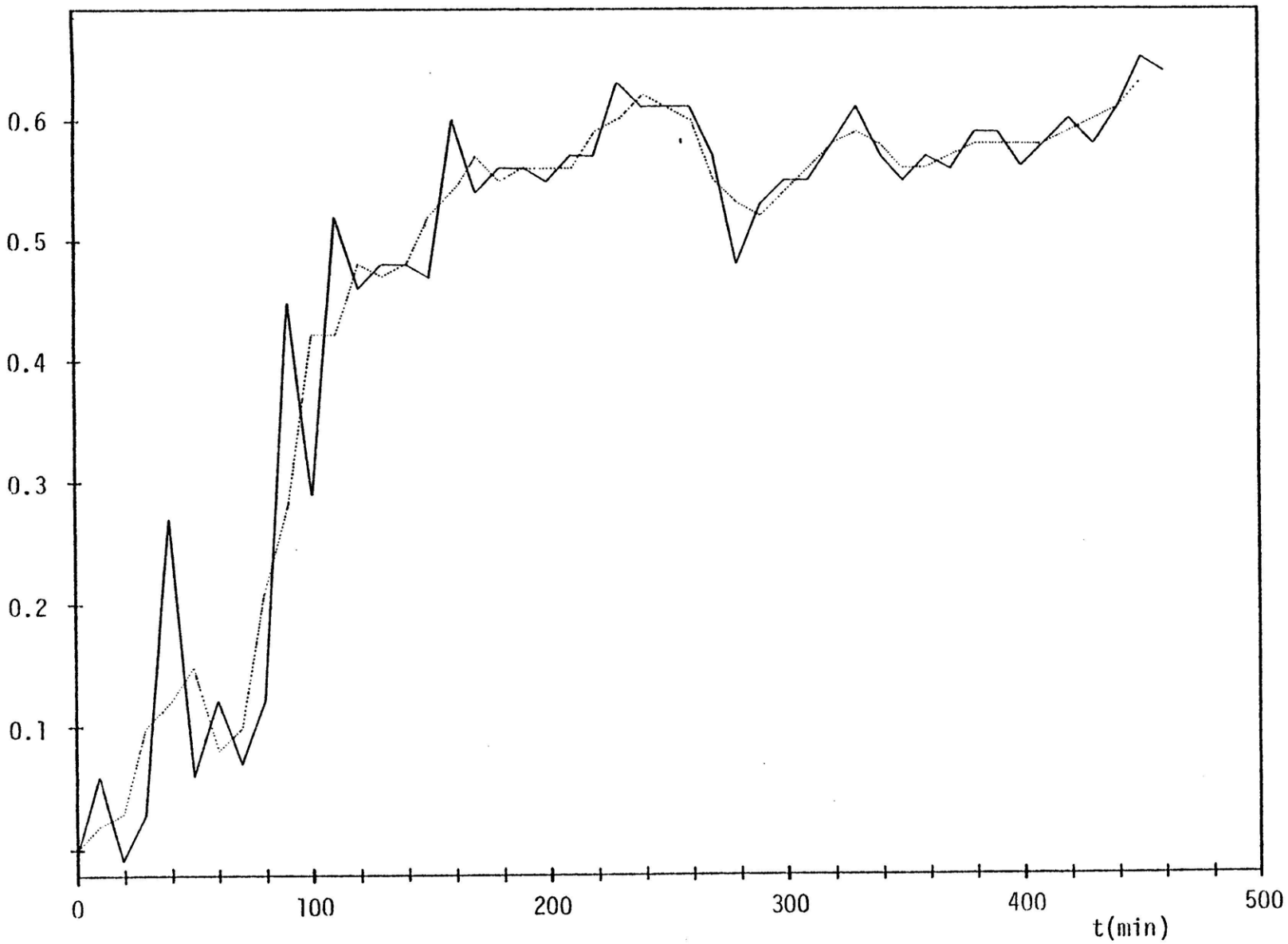

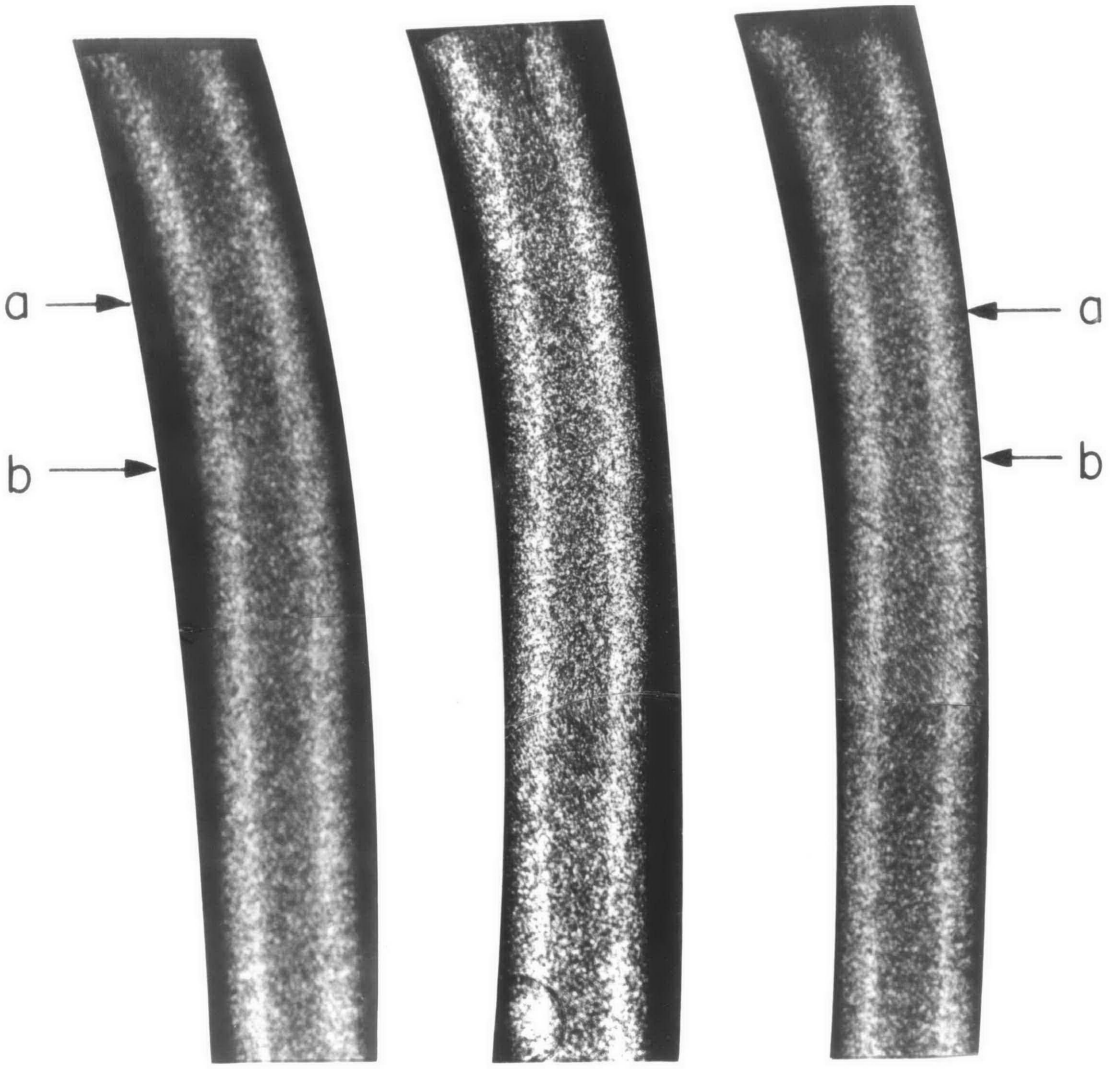

Figure 2.10 The Injector Blockage Configuration
(magnified 50 times)

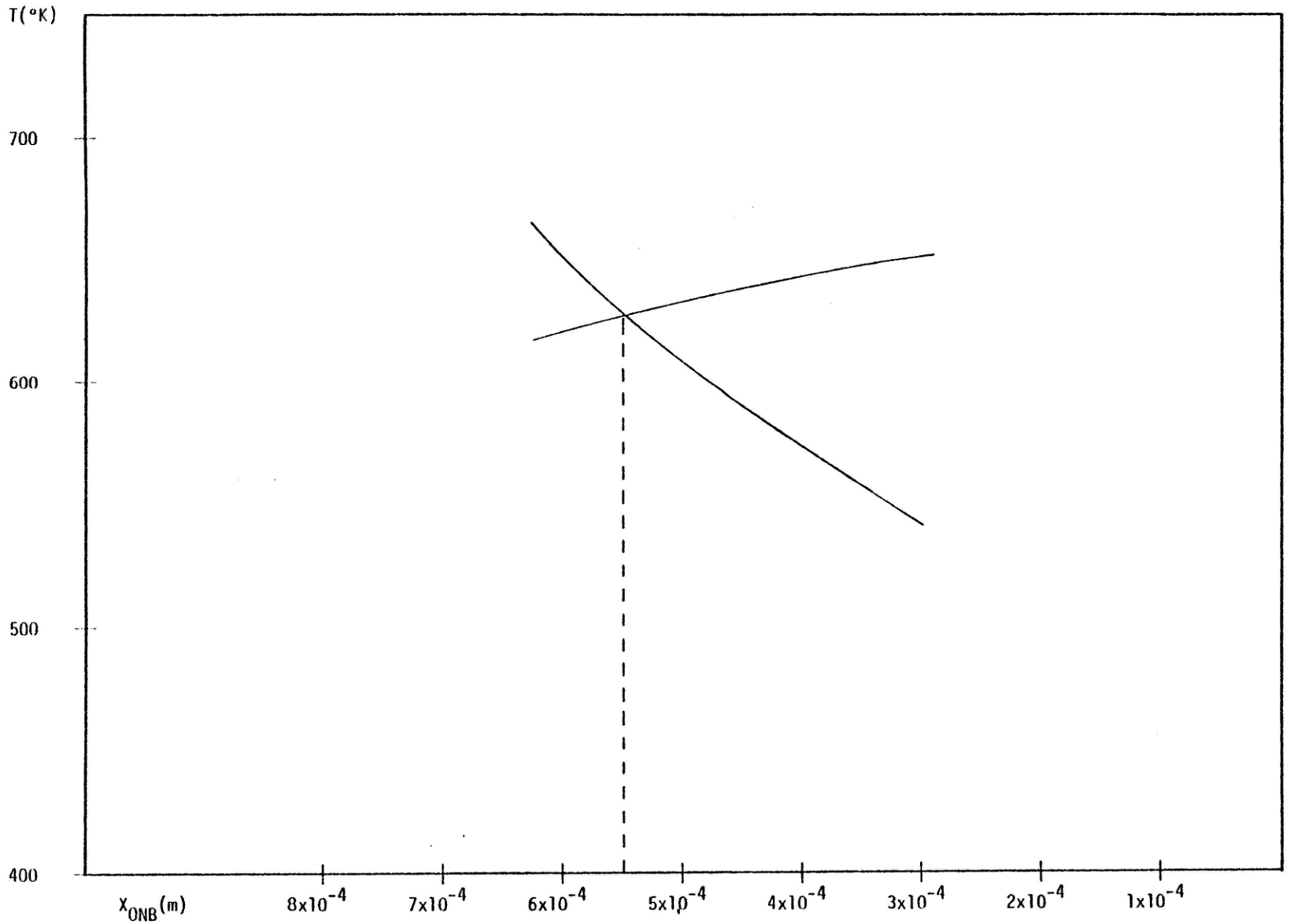

Figure 2.11 Determination of X_{ONB} Point and T_0

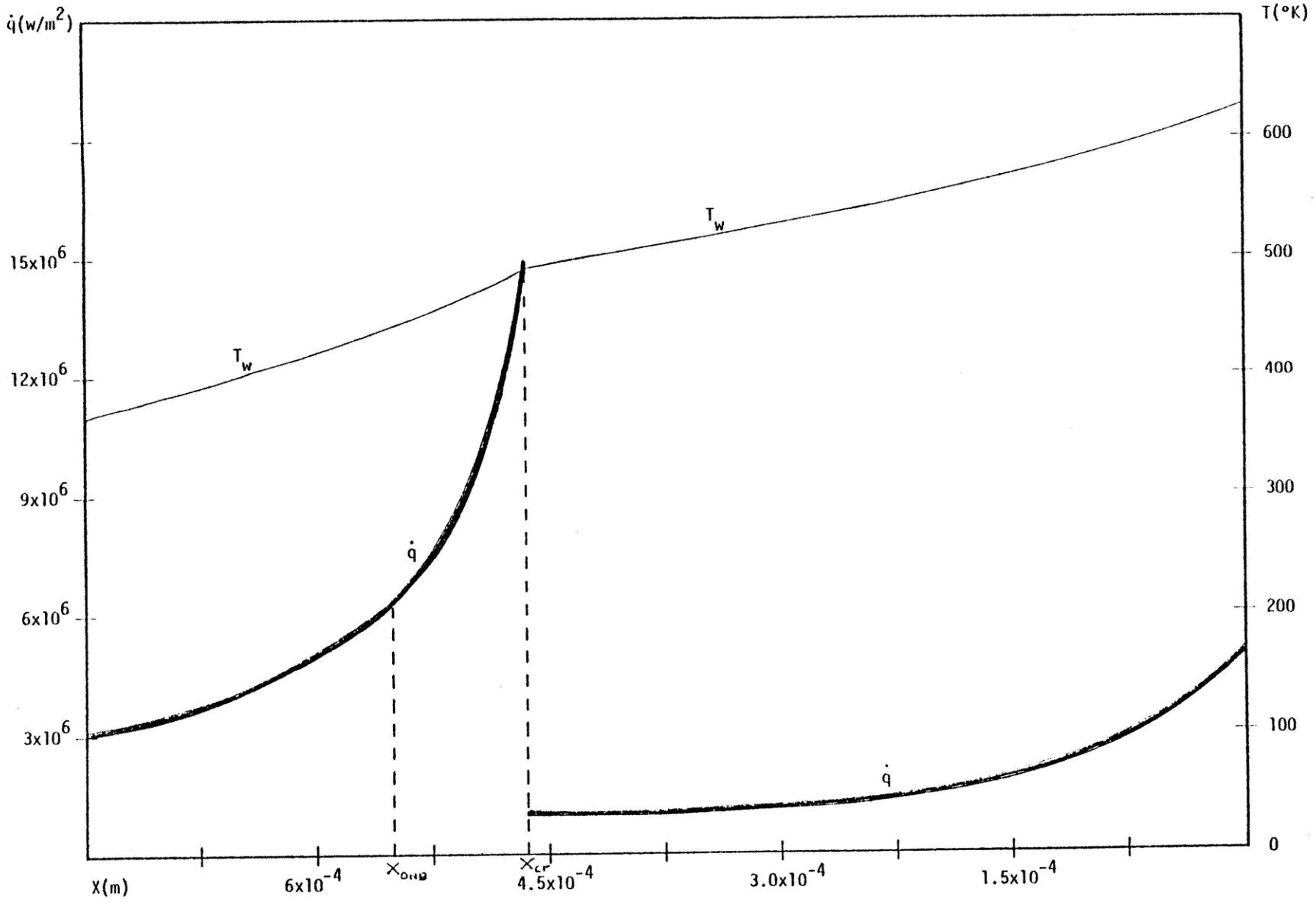

Figure 2.12 Heat Flux and Temperature Distribution

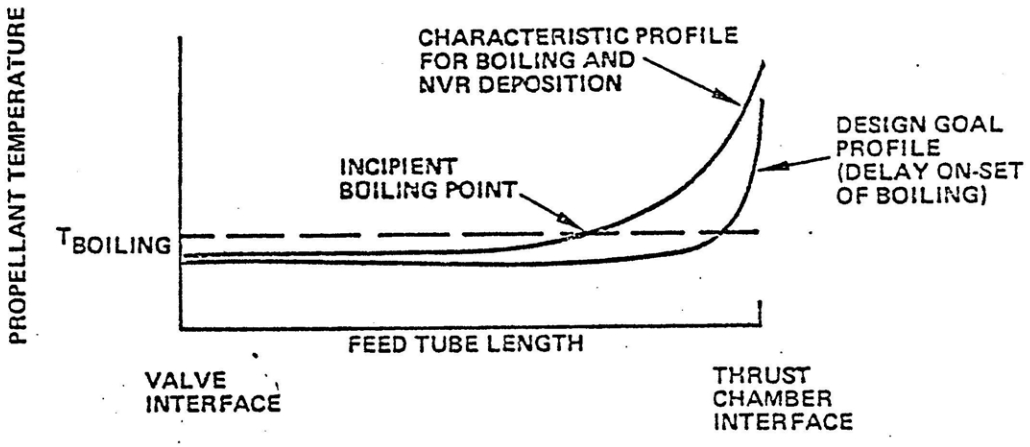

Figure 2.13 Feed Tube Propellant Temperature Profiles (From reference (1))